Published in final edited form as:
IEEE Trans Med Imaging. 2009 October ; 28(10): 1526–1533. doi:10.1109/TMI.2009.2019823.

Shear modulus decomposition algorithm in Magnetic Resonance Elastography

Oh In Kwon, **Chunjae Park**, **Hyun Soo Nam**, **Eung Je Woo [Member, IEEE]**, **Jin Keun Seo**, **K.J. Glaser**, **A. Manduca**, and **R.L. Ehman**

Abstract

Magnetic resonance elastography (MRE) is an imaging modality capable of visualizing the elastic properties of an object using MRI measurements of transverse acoustic strain waves induced in the object by a harmonically oscillating mechanical vibration. Various algorithms have been designed to determine the mechanical properties of the object under the assumptions of linear elasticity, isotropic and local homogeneity. One of the challenging problems in MRE is to reduce the noise effects and to maintain contrast in the reconstructed shear modulus images. In this paper, we propose a new algorithm designed to reduce the degree of noise amplification in the reconstructed shear modulus images without the assumption of local homogeneity. Investigating the relation between the measured displacement data and the stress wave vector, the proposed algorithm uses an iterative reconstruction formula based on a decomposition of the stress wave vector. Numerical simulation experiments and real experiments with agarose gel phantoms and human liver data demonstrate that the proposed algorithm is more robust to noise compared to standard inversion algorithms and stably determines the shear modulus.

Index Terms

Magnetic resonance elastography; shear modulus; elasticity; MRI

I. Introduction

Using magnetic resonance imaging (MRI) techniques, magnetic resonance elastography (MRE) measures the propagation of transverse acoustic strain waves in an object of interest (Muthupillai *et al.* [11]). By measuring the propagating strain waves, the aim of MRE is to extract useful information about the elastic mechanical properties of the object. Various algorithms have been developed to reconstruct the shear modulus distributions inside the imaged object ([10], [14], [20], [23], [24], [26], [27]).

The propagation speed of harmonic mechanical waves can be derived from the wave equation, which in turn depends on the underlying stress-strain relationship of the support medium. In general, soft tissues are mechanically anisotropic, viscoelastic and have nonlinear displacement characteristics. However, we assume that the materials behave as linearly elastic and isotropic materials to image the shear modulus distribution. The linear elasticity assumption is used in MRE because the mechanical wave motion studied is very small (typically tens of microns), and the assumption of an isotropic medium simplifies the equations of motion. Denoting the elastic displacement field by $\mathbf{u} = (u_1, u_2, u_3)$, this leads to the partial differential equation governing time-harmonic, isotropic, linearly elastic motion ([4], [5], [24]):

$$\nabla \cdot ((\mu + i\omega\zeta)\nabla \mathbf{u}) + \nabla((\lambda + \mu)\nabla \cdot \mathbf{u}) = -\rho\omega^2 \mathbf{u} \quad (1)$$

where ρ is the tissue density, λ the Lamé parameter, which is related with the elastic resistance to the volume change, ζ the shear viscosity, and μ the shear modulus describing the tissue's elastic resistance to shape change.

Most of conventional approaches for the shear modulus parameter identification problem make some assumptions to reduce the equations of elasto-dynamics down to the Helmholtz equation in order to take advantage of requiring a single measurement of displacement field for the reconstruction ([8], [14], [15], [20], [22], [26], [27]). These assumptions may cause some inaccuracy in the reconstruction of μ due to the presence of a substantial fraction of compressional wave in the total displacement [19]. Assuming that the tissue is nearly incompressible, one may approximate $\nabla \cdot ((\mu + i\omega\zeta)\nabla \mathbf{u}) = -\rho\omega^2\mathbf{u} - \nabla((\lambda + \mu)\nabla \cdot \mathbf{u}) \approx -\rho\omega^2\mathbf{u} - \mu\mathbf{u}_L$ where $\mathbf{u}_L$ is a curl-free part of $\mathbf{u}$ ([24]). If we further assume that $\rho\omega^2$ is much higher than μ, then the equation (1) simplifies to the Helmholtz equation([8], [14], [15]):

$$\nabla \cdot ((\mu + i\omega\zeta)\nabla u_i) = -\rho\omega^2 u_i, \quad i = 1, 2, 3 \qquad (2)$$

Therefore, one component measurement of the displacement field can be used to determine the mechanical property μ, which can be solved locally by direct algebraic inversion methods under the assumption of local homogeneity ([7], [8], [9], [10], [12], [13], [14]):

$$\mu + i\omega\zeta = -\rho\omega^2 \frac{u_i}{\nabla^2 u_i} \qquad (3)$$

Here, the density ρ is assumed to be a constant value (1000 kg/m^3), which is typical of a soft tissue ([2]). The conventional direct algebraic inversion method can immediately depict the interior elasticity distribution in the object (called an elastogram), even from only one component of the full vector displacement data.

One drawback of the direct algebraic inversion method (3) is that double differentiation of the measured displacement data u_i can cause undesirable noise effects owing to the tendency of the operations to amplify noise. To alleviate the noise amplification from measured data, this method typically needs some filtering to reduce the high-frequency noise ([10]). Another drawback of this method is that the modeling error from the assumption of local homogeneity produces artifacts around regions of differing elastic properties even with noiseless data.

The aim of this paper is to present a new method for reconstructing shear modulus images without the assumption of local homogeneity and requiring single differentiation of data only. The new algorithm, called a shear modulus decomposition algorithm, that is designed to avoid noise amplification caused by the double derivatives of the measured data and to maintain contrast information in the reconstructed shear modulus images. Investigating the relation between the measured displacement data and the stress wave vector, we decomposes the stress wave vector into a curl-free, a divergence-free, and a harmonic part so that the curl-free part is computable directly from the measured displacement data and extracts the principle information about the shear modulus.

In the proposed algorithm, we first reconstruct a principal component μ^* of the shear modulus μ using the recovered curl-free part of the stress wave vector. This decomposed μ^* itself is a reasonable approximation of μ. Next, we recover small missing information in $\mu - \mu^*$ using the divergence-free part of the stress wave vector by the way of an iterative procedure.

Numerical experiments and phantom experiments show that the shear modulus decomposition algorithm considerably improves the quality of the reconstructed shear modulus image from noisy measured displacement data compared to the algebraic inversion algorithm in (3). We analyze the dependence of the displacement SNR via the addition of zero-mean Gaussian random noise and its effect on the reconstructed shear modulus image. The proposed algorithm is also tested with real experimental data including human liver data. The proposed algorithm based on the simplified equation (2) neglects the hydrostatic stress term. To observe the effect of the hydrostatic stress term, we recovered and compared the shear modulus images by using the shear modulus decomposition algorithm with displacement field which were generated by solving the elasticity system (1) in a two dimensional domain. In this paper, we focused on recovering the shear modulus μ, but we can also recover the viscoelastic value ζ simultaneously. The recovered viscoelastic image using phantom experiments are displayed and discussed.

II. Methods

A. Shear modulus decomposition algorithm

The equation (2) can be written as

$$\nabla \cdot ((\mu+i\omega\zeta)\nabla u_i)=(\mu+i\omega\zeta)\nabla^2 u_i+\nabla(\mu+i\omega\zeta)\cdot\nabla u_i=-\rho\omega^2 u_i, \quad i=1,2,3 \quad (4)$$

Hence, the reconstruction formula (3) neglects the term $\nabla(\mu+i\omega\zeta)\cdot\nabla u_i$ representing a local change of $\mu+i\omega\zeta$ in the direction ∇u_i. In order to probe any local contrast of μ, it would be desirable to include the effect of $\nabla(\mu + i\omega\zeta)\cdot\nabla u_i$.

According to the Helmholtz-Hodge decomposition, the vector field $(\mu + i\omega\zeta)\nabla u_i$ in the equation (2) can be decomposed into a curl-free component, a divergence-free component, and a harmonic term. In particular, it can be written as

$$(\mu+i\omega\zeta)(\mathbf{r})\nabla u_i(\mathbf{r})=\nabla f_i(\mathbf{r})+\nabla\times W_i(\mathbf{r})+\nabla h_i(\mathbf{r}) \quad \text{in } \mathscr{R} \quad (5)$$

where $\mathscr{R}$ is a region to be imaged, f_i and W_i are respectively solutions of the the following problems

$$\begin{cases} \nabla^2 f_i(\mathbf{r})=-\rho\omega^2 u_i(\mathbf{r}), & \mathbf{r}\in\mathscr{R} \\ \nabla f_i(\mathbf{r})\cdot\nu=\frac{\rho\omega^2 u_i}{\nabla^2 u_i}\nabla u_i(\mathbf{r})\cdot\nu+\alpha, & \mathbf{r}\in\partial\mathscr{R} \end{cases} \quad (6)$$

and

$$\begin{cases} \nabla^2 W_i(\mathbf{r})=\nabla(\mu+i\omega\zeta)\times\nabla u_i(\mathbf{r}), & \mathbf{r}\in\mathscr{R} \\ \nabla W_i(\mathbf{r})\times\nu=0, & \mathbf{r}\in\partial\mathscr{R} \end{cases} \quad (7)$$

and h_i is a harmonic function satisfying

$$\begin{cases} \nabla^2 h_i(\mathbf{r})=0, & \mathbf{r}\in\mathscr{R} \\ \nabla h_i(\mathbf{r})\cdot\nu=\left((\mu+i\omega\zeta)-\frac{\rho\omega^2 u_i}{\nabla^2 u_i}\right)\nabla u_i(\mathbf{r})\cdot\nu-\alpha, & \mathbf{r}\in\partial\mathscr{R} \end{cases} \quad (8)$$

where ν is the outer normal unit vector on the boundary and α is a constant such that $\alpha = (\text{the surface area of the boundary})^{-1} \times \left(\int_{\mathcal{R}} \rho\omega^2 u_i d\mathbf{r} - \int_{\partial\mathcal{R}} \frac{\rho\omega^2 u_i}{\nabla^2 u_i} \nabla u_i \cdot \nu ds \right)$. Here, $\partial\mathcal{R}$ denotes the boundary of $\mathcal{R}$. The constant α is needed for the existence of solutions of (6) and (8).

The direct inversion method in (3) which ignores the effect of $\nabla(\mu + i\omega\zeta) \cdot \nabla u_i$ is equivalent to the identity

$$\mu = \mathcal{R}e\left\{\frac{\nabla^2 f_i}{\nabla^2 u_i}\right\} \quad \text{and} \quad \zeta = \frac{1}{\omega}\mathcal{I}m\left\{\frac{\nabla^2 f_i}{\nabla^2 u_i}\right\} \tag{9}$$

since it makes the approximation $\nabla^2 f_i = (\mu + i\omega\zeta)\nabla^2 u_i + \nabla(\mu + i\omega\zeta)\cdot\nabla u_i \approx (\mu + i\omega\zeta)\nabla^2 u_i$. Here, $\mathcal{R}e\{\cdot\}$ and $\mathcal{I}m\{\cdot\}$ denote the real and imaginary part. Under noise conditions with the measured data u_i, any reconstruction algorithm using the formula (9) has a problem in providing high spatial resolution images of μ due to noise amplification by the double differentiation of u_i. Hence, in order to obtain better resolution image of μ, it would be desirable to reduce the noise amplification effect of the double differentiation of u_i and to include the influence of $\nabla(\mu + i\omega\zeta) \cdot \nabla u_i$ in a reconstruction algorithm.

To reduce the noise amplification effect in the computation of $\nabla^2 u_i$ in (9), we use the formula (5) which requires single differentiation only. Taking the inner product of ∇u_i on both sides of the identity (5) leads to the following formula

$$\mu + i\omega\zeta = \frac{\nabla f_i \cdot \nabla \bar{u}_i + \nabla \times W_i \cdot \nabla \bar{u}_i + \nabla h_i \cdot \nabla \bar{u}_i}{\nabla u_i \cdot \nabla \bar{u}_i} \tag{10}$$

where $\bar{u}_i$ is the complex conjugate of u_i. The quantity ∇f_i can be computed using a standard numerical method because the boundary value problem (6) is a Poisson equation with the known source term $\rho\omega^2 u_i$ and the known Neumann data. However, $\nabla \times W_i$ and ∇h_i are related to the unknown quantity $\mu + i\omega\zeta$ since $\nabla \times W_i$ is determined by the quantity $\nabla(\mu + i\omega\zeta) \times \nabla u_i$ according to (7) and ∇h_i is determined by the difference $\mu + i\omega\zeta - \frac{\rho\omega^2 u_i}{\nabla^2 u_i}$ on the boundary $\partial\mathcal{R}$. Fortunately, it is notable that $\nabla h_i \approx 0$ inside $\mathcal{R}$ (except near the boundary $\partial\mathcal{R}$) since the function h_i is harmonic inside $\mathcal{R}$ and the boundary data of $\frac{\partial h_i}{\partial \nu}$ is oscillating at high frequency with zero mean on the boundary $\partial\mathcal{R}$. See Appendix for a detailed analysis and a numerical simulation. Therefore, we may ignore the term $\nabla h_i \cdot \nabla \bar{u}_i$ in the identity (10).

Now, we have a new approximation for the shear modulus:

$$\mu + i\omega\zeta = \frac{\nabla f_i \cdot \nabla \bar{u}_i}{\nabla u_i \cdot \nabla \bar{u}_i} + \frac{\nabla \times W_i \cdot \nabla \bar{u}_i}{\nabla u_i \cdot \nabla \bar{u}_i} \tag{11}$$

The first quantity in (11) can be viewed as *the prime component of the shear modulus* μ. We denote it as μ^*:

$$\mu^* = \mathcal{R}e\left\{\frac{\nabla f_i \cdot \nabla \bar{u}_i}{\nabla u_i \cdot \nabla \bar{u}_i}\right\} \quad \text{and} \quad \zeta^* = \frac{1}{\omega}\mathcal{I}m\left\{\frac{\nabla f_i \cdot \nabla \bar{u}_i}{\nabla u_i \cdot \nabla \bar{u}_i}\right\} \tag{12}$$

As will be shown Fig. 4 and Fig. 7 in Section III, the leading component μ^* itself is a good approximation of the true μ. To achieve an even more accurate reconstruction, we need to use the second term involving $\nabla \times W$ in (11) which takes account of the curl effect $\nabla(\mu +$

$i\omega\zeta) \times \nabla u$. Taking advantage of the known μ^* and ζ^*, we can update the shear modulus value by using a natural iterative procedure. Let W_i^1 be the solution of (7) with $\nabla(\mu + i\omega\zeta)$ replaced by $\nabla(\mu^* + i\omega\zeta^*)$. We compute μ_1:

$$\mu^1 = \mu^* + \mathscr{R}e\left\{\frac{\nabla \times W_i^1 \cdot \nabla \overline{u}_i}{\nabla u_i \cdot \nabla \overline{u}_i}\right\} \quad (13)$$

For each $n = 2, \cdots$, we denote W^n by the solution of (7) with $\nabla(\mu + i\omega\zeta)$ replaced by $\nabla(\mu^{n-1} + i\omega\zeta^{n-1})$ and update the shear modulus value iteratively:

$$\mu^n = \mu^* + \mathscr{R}e\left\{\frac{\nabla \times W_i^n \cdot \nabla \overline{u}_i}{\nabla u_i \cdot \nabla \overline{u}_i}\right\} \quad (14)$$

If we have the three components of displacement (u_1, u_2, u_3), the the shear modulus μ^* in (12) can be determined by

$$\mu^* = \frac{\sum_{i=1}^3 \mathscr{R}e\{\nabla f_i \cdot \nabla \overline{u}_i\}}{\sum_{i=1}^3 \nabla u_i \cdot \nabla \overline{u}_i} \quad (15)$$

and the following iterative procedure can be applied:

$$\mu^n = \mu^* + \frac{\sum_{i=1}^3 \mathscr{R}e\{\nabla \times W_i^n \cdot \nabla \overline{u}_i\}}{\sum_{i=1}^3 \nabla u_i \cdot \nabla \overline{u}_i} \quad (16)$$

The proposed gradient component of stress based inversion algorithm proceeds as follows:

I. **a.** Compute the gradient part ∇f_i of $(\mu + i\omega\zeta)\nabla u_i$ by solving (6).

b. Reconstruct the component μ^* of the shear modulus μ by (15) using ∇f_i and the data u_i.

II. **a.** Set $\mu^0 = \mu^*$. For each $n = 1, 2, \cdots$, compute μ_n in the following way:

i. Compute $\nabla \times W_i^n$ by solving (7) with $\nabla(\mu + i\omega\zeta)$ replaced by $\nabla(\mu^{n-1} + i\omega\zeta^{n-1})$.

ii. Update μ^n using (16) with the updated curl part $\nabla \times W_i^n$

b. Stop the process if $\frac{\left\|\mu^n - \mu^{n-1}\right\|}{\left\|\mu^n\right\|} \leq \varepsilon$ where $\varepsilon > 0$ is a given tolerance and $\|\cdot\|$ is a standard L^2-norm. Otherwise, repeat the process with $n = n + 1$.

B. Noise tolerance of μ*

To verify the proposed method and to investigate its tolerance to noise, numerical simulations and real experiments involving gel phantoms and in vivo liver tissue were performed.

With noisy measured data u_i, the decomposed shear modulus μ^* in (15) can be written as

$$\mu^* = \frac{\sum_{i=1}^{3} \mathcal{R}e\{(\nabla f_i + \varepsilon_{\nabla f_i}) \cdot (\nabla \overline{u}_i + \varepsilon_{\nabla u_i})\}}{\sum_{i=1}^{3} \mathcal{R}e\{(\nabla u_i + \varepsilon_{\nabla u_i}) \cdot (\nabla \overline{u}_i + \varepsilon_{\nabla u_i})\}}. \quad (17)$$

where $\varepsilon_{\nabla u_i}$ and $\varepsilon_{\nabla f_i}$ are the noises in the derivative estimates involving u_i and f_i, respectively. The noise standard deviations $sd(\varepsilon_{\nabla u_i})$ and $sd(\varepsilon_{\nabla f_i})$ are proportional to $\frac{sd(u_i)}{\Delta}$ and $\frac{sd(f_i)}{\Delta}$, respectively, where Δ is the pixel size of the image. We note that $sd(f_i)$ is less than $sd(u_i)$ because two derivatives of f_i returns us to the noise level of the original measured displacement data. Using the terminology $g(\varepsilon) = \mathcal{O}(\varepsilon)$, which means that the ratio $\frac{g(\varepsilon)}{\varepsilon}$ stays bounded as $\varepsilon \to 0$, the shear modulus μ is influenced by

$$\begin{aligned} \mu^* &= \frac{\sum_{i=1}^{3} \mathcal{R}e\{\nabla f_i \cdot \nabla \overline{u}_i + \mathcal{O}(\varepsilon_{\nabla f_i}) + \mathcal{O}(\varepsilon_{\nabla u_i})\}}{\sum_{i=1}^{3} \nabla u_i \cdot \nabla \overline{u}_i + \mathcal{O}(\varepsilon_{\nabla u_i})} \\ &= \frac{1}{\sum_{i=1}^{3} \nabla u_i \cdot \nabla \overline{u}_i} \frac{\sum_{i=1}^{3} \mathcal{R}e\{\nabla f_i \cdot \nabla \overline{u}_i\} + \mathcal{O}(\varepsilon_{\nabla f_i}) + \mathcal{O}(\varepsilon_{\nabla u_i})}{1 + \mathcal{O}(\varepsilon_{\nabla u_i})} \\ &= \frac{\sum_{i=1}^{3} \mathcal{R}e\{\nabla f_i \cdot \nabla \overline{u}_i\}}{\sum_{i=1}^{3} \nabla u_i \cdot \nabla \overline{u}_i} + \mathcal{O}(\varepsilon_{\nabla f_i}) + \mathcal{O}(\varepsilon_{\nabla u_i}). \end{aligned} \quad (18)$$

Hence, the proposed algorithm evaluating μ^* has an error term of order $\mathcal{O}\left(\frac{sd(u_i)}{\Delta}\right)$, while the direct inversion method has an error term of order $\mathcal{O}\left(\frac{sd(u_i)}{\Delta^2}\right)$. This means that the relation (18) implies that the proposed algorithm substantially reduces the noise effect on the reconstructed shear modulus image compared to the noise level of the conventional direct inversion method.

C. Numerical simulation

To test the gradient component of stress based inversion algorithm, we performed a numerical simulation for a two-dimensional model in the region $\mathcal{R} = 20 \times 20\ \text{cm}^2$ with the origin at its bottom-left. We used a finite element method and discretized the rectangular model with 128 × 128 four-node rectangle elements with bilinear interpolation functions. Fig. 2(a) shows the image of the simulated target shear modulus. The target shear modulus included eight disks of different diameters with shear moduli $\mu = 2$ kPa and the background shear modulus is $\mu_0 = 1$ kPa. We added viscosity material property in the simulated model; eight disks and the background include 15 Pa and 3 Pa, respectively. We generated the simulated displacement data u by solving the simplified wave equation (2) with $\frac{\omega}{2\pi} = 40$ Hz and the boundary condition given by

$$\begin{cases} u = 1, & \text{if } y = 20, |x - 10| \le 4, \\ u = 0, & \text{if } y = 0, |x - 10| \le 10, \\ \nabla u \cdot \nu = 0 & \text{on the other boundary} \end{cases}$$

The figure 2(b) and (c) are the real and imaginary parts of the simulated displacement field, respectively.

In order to test the noise tolerance of the algorithm, we added 2% and 4% Gaussian random noise with respect to the maximum intensity to the simulated displacement data u. For the study of the reconstruction characteristics of the proposed algorithm, we defined the relative L^2-error of the reconstructed shear modulus images in $\mathcal{R}$ as

$$E_{\mu^r} \equiv \frac{\|\mu - \mu^r\|}{\|\mu\|} = \sqrt{\frac{\int_{\mathcal{R}} |\mu(\mathbf{r}) - \mu^r(\mathbf{r})|^2}{\int_{\mathcal{R}} |\mu(\mathbf{r})|^2}} \quad (19)$$

where μ and μ^r denote the specified and the reconstructed shear modulus images in $\mathcal{R}$, respectively.

D. Real data experiments

Phantom experiments were performed to compare the shear modulus decomposition algorithm to the conventional direct inversion. An agarose gel phantom containing four cylindrical inclusions of stiffer gel was studied in a 1.5T MR scanner (General Electric, Milwaukee, WI). The outside gel was 1.5% agar and the cylinders were composed of 10% B-gel (bovine) to create a contrast in the shear modulus. The diameters of the four cylindrical objects were approximately 5, 10, 16, and 25 mm. Three-dimensional data acquisitions were performed. The *z*-direction phase difference image was acquired using a tetrahedral 3D GRE MRE scan and eight offsets through time were acquired. The reconstructed image matrix was 256 × 256 × 16 with a FOV of 20 × 20 cm^2 and 3 mm slice thickness. From separate reference phantoms, the shear modulus of the background was estimated to be 2.9 kPa and the stiff inclusions were 6.4 kPa. Vibrations at 100 Hz were introduced into the phantom via an electromechanical actuator placed on top of the phantom that oscillated in the *z*-direction. The *z*-direction is parallel to the cylindrical inclusions and the 8-th imaging slice was located at the center of the phantom along the *z*-axis.

To further demonstrate the capabilities of the shear modulus decomposition algorithm, the technique was also studied in the case of a patient undergoing a liver MRE exam. The patient data were acquired using a previously documented liver MRE protocol approved by the Mayo Clinic IRB([28]) which will be briefly summarized. After obtaining informed consent, the patient was imaged in the supine position. Motion was introduced into the abdomen using an active pressure system coupled to a passive drum placed on the chest wall of the patient. The motion was applied at 60 Hz and axial images of the mechanical vibrations in the liver were obtained using a 36 cm FOV, 256 ×64 acquisition matrix reconstructed to 256 × 256, and 4 phase offsets with motion-encoding gradients applied in the through-plane direction. Fig. 3(a) shows an MR magnitude image of the imaging slice and Fig. 3(b–c) show the corresponding real and imaginary displacement images. The FOV is 36 × 36 cm^2 with matrix size 256 × 256. We set the excitation frequency at 60 Hz. In these phantom and in vivo human liver experiments, the imaging objects are compactly supported in FOV.

III. RESULTS

A. Simulation results

Fig. 4 shows the results from the simulation study. The upper row in Fig. 4 shows the reconstructed shear modulus images using the conventional direct inversion algorithm for noiseless case, and for the data with 2%, and 4% added random noise, respectively. The second row in Fig. 4 shows μ^* that is computed by the direct formula (12). The third row in Fig. 4 shows the reconstructed shear modulus μ^4 after four iterations using the proposed gradient component of stress based algorithm.

In the shear modulus reconstruction process in the inversion algorithms, the single and double derivatives were approximated by the differential templates:

$$\frac{\partial}{\partial x}=\frac{1}{8\Delta}\begin{bmatrix}-1 & 0 & 1\\ -2 & 0 & 2\\ -1 & 0 & 1\end{bmatrix} \quad \text{and} \quad \frac{\partial}{\partial y}=\frac{1}{8\Delta}\begin{bmatrix}1 & 2 & 1\\ 0 & 0 & 0\\ -1 & -2 & -1\end{bmatrix} \tag{20}$$

and

$$\frac{\partial^2}{\partial x^2}=\frac{1}{4\Delta^2}\begin{bmatrix}1 & -2 & 1\\ 2 & -4 & 2\\ 1 & -2 & 1\end{bmatrix} \quad \text{and} \quad \frac{\partial^2}{\partial y^2}=\frac{1}{4\Delta^2}\begin{bmatrix}1 & 2 & 1\\ -2 & -4 & -2\\ 1 & 2 & 1\end{bmatrix}. \tag{21}$$

To compare the performance of the two algorithms using noisy data, no denoising techniques or smoothing of the data was used. Fig. 4(a–c) show the recovered shear modulus images using the direct inversion method (3) with the displacement data containing 0%, 2%, and 4% random noise, respectively. There are some artifacts near the edges of the inclusions even for noise-free data. The images are distorted in the region where the vector $\nabla\mu$ is parallel to the vector ∇u.

Fig. 4(d–f) show the reconstructed μ^* of the shear modulus whose values are slightly lower than the specified value. These results compared to Fig. 4(a–c) indicate that the shear modulus decomposition algorithm (12) is more robust to noise than the direct inversion method (3).

Fig. 4(g–i) show the the reconstructed shear modulus μ^4 in (14) with four iterations. This iteration compensates the information of $\nabla \times W$, where the computation of W requires to solve the elliptic partial equation (7). Table 1 shows the relative errors E_{μ^r} via (19) for each reconstructed shear modulus image.

Fig. 5 shows profiles from the shear modulus images in Fig. 4 along the horizontal line y = 12. The profile image in Fig. 5(a) using the direct inversion method on the noiseless data shows that inside the larger constant shear modulus regions provided nearly the correct values, but there were some artifacts around the edges of the inclusions. The images in Fig. 5(c),(f), and (i) show that the shear modulus decomposition algorithm suppresses the noise amplification in the reconstructed shear modulus images while maintaining high resolution.

B. Phantom experimental results

Fig. 6(a) shows the measured z-sensitized displacement image of the phantom data for the middle (8-th) slice. Since the measured displacement shows some interference patterns caused by the cylinders and the boundaries of the phantom, a spatio-temporal filter was designed in frequency space to select portions of the wave field propagating in specific directions. Even though the recovered waves using these frequency domain filters are not physically realistic, they still satisfy the original wave equation. The filter was designed to cut off very low and very high frequencies to select only waves propagating down through the phantom ([10]). Fig. 6(b) shows the wave field after the application of directional filter. We used the z-sensitized displacement data in Fig. 6 and calculated the reconstructed shear modulus images in the three dimension by solving a three dimensional finite element method.

Fig. 7(a–c) and (d–f) show the reconstructed shear modulus using the measured displacement data with and without directional filtering, respectively. The direct inversion results are shown in Fig. 7(a) and (d). The results in the second and third columns in Fig. 7 using the proposed algorithm correspond to μ^* and μ^4, respectively. The reconstructed

images show that the proposed algorithm has the potential to improve the image quality and contrast of nondirectional filtered data compared to the direct inversion algorithm. The direct inversion results in Fig. 7 included smoothing with a spatial window of 11 × 11 to suppress the noise amplification.

In this phantom experimental setup, the waves mainly propagate downward. However, the reconstructed images using the filtered data, which suppresses the low-frequency compressional waves, the high-frequency noise, and waves interfering with the primary wavefront, have fewer artifacts than those using the nondirectional filtered data.

Fig. 8 shows profiles through the four inclusions from the results in Fig. 7. Fig. 8(a–c) are the results without directional filtering using the direct inversion method and the gradient component of stress based method, respectively. Fig. 8(d–f) are the corresponding profiles with the directionally filtered data. The profiles in figure 8 show that the reconstructed stiffnesses of the four inclusions using the direct inversion are missing resolution of the small inclusions by using the surround window to take double derivatives. However, those using the gradient component of stress based algorithm show that the proposed algorithm can produce higher resolution shear modulus images and more uniform contrast compared to the direct inversion algorithm. The inclusion stiffnesses in the reconstructed shear modulus image μ^* in Fig. 8(b) and (e) were slightly lower than that of the true value of 6.4 kPa. The reason may come from the assumption of local homogeneity which neglects $\nabla \times W$ in (5).

For the in vivo human liver experiment, Fig. 9(a) shows a subset of the MR magnitude image indicating the patient anatomy with the two tumors highlighted with two circles and identified as R_1 and R_2. Fig. 9(b) and (c) show the magnitude image again with two rectangular overlays indicating the domains defined for the shear modulus decomposition of the two tumors. The overlays in Fig. 9(b) and (c) are the real and imaginary part images of the potential function f in the two local regions obtained by solving the elliptic equation (6) with the measured displacement data as source terms and Neumann boundary conditions on the boundary of the two local regions. Fig. 10(a) shows the full MR magnitude image with the results from the shear modulus decomposition algorithm overlayed in the two rectangular insets, and Fig. 10(b) is the corresponding shear modulus image for the whole field of view using the direct inversion algorithm. The two reconstructed images show common characteristics, but as expected, the reconstructed image using the proposed algorithm shows the tumors with better contrast, uniformity, and resolution than the direct inversion method. The average values of the shear modulus inside the two circled regions are 3.47 kPa in R_1 and 3.26 kPa in R_2 when we used the usual direct inversion algorithm. We obtained 3.19 kPa in R_1 and 3.40 kPa in R_2 using the proposed algorithm.

IV. DISCUSSION

The numerical results presented in this work show that the shear modulus decomposition algorithm successfully reconstructs shear modulus images from scalar displacement data with added Gaussian random noise. The novelty of the proposed algorithm is that it requires a single differentiation of the measured displacement to reconstruct the chief component μ^* of the shear modulus, which is a good approximation (or good initial guess) of the true μ. The small missing information in $\mu - \mu^*$ is related to the curl part $\nabla \times W_i$ in (5) which satisfies

$$\nabla \times \nabla \times W_i = \nabla(\mu + i\omega\zeta) \times \nabla u_i. \quad (22)$$

The component μ^* in Fig. 8(b) and (e) slightly underestimated the measured shear modulus value of 6.4 kPa for the inclusions. This lower value of μ^* may be caused by ignoring the curl part $\nabla \times W_i$.

To compensate for the missing divergence-free part $\nabla \times W_i$ of $(\mu + i\omega\zeta)\nabla u_i$, the shear modulus is iteratively updated by solving (7) with the updated source term $\nabla(\mu^n + i\omega\zeta^n) \times \nabla u_i$. The reconstructed simulation results in Fig. 4 show different characteristics between the direct inversion algorithm and the proposed algorithm even with the noiseless simulated displacement data. In the direct inversion algorithm based on (3), the local homogeneity assumption produces artifacts in the regions where the modulus gradient $\nabla\mu$ is parallel to the direction ∇u_i since its algorithm neglects the term $\nabla(\mu+i\omega\zeta)\cdot\nabla u_i$, which can be viewed as the ∇u_i-directional change of $\mu + i\omega\zeta$, by the rough approximation:

$$\nabla \cdot ((\mu+i\omega\zeta)\nabla u_i)=\nabla(\mu+i\omega\zeta) \cdot \nabla u_i+(\mu+i\omega\zeta)\nabla^2 u_i \approx (\mu+i\omega\zeta)\nabla^2 u_i. \quad (23)$$

The proposed algorithm takes account of the term $\nabla(\mu + i\omega\zeta) \cdot \nabla u_i$ and produces a more uniform depiction.

Since a human body is characterized by possessing both viscous and elastic behaviors, viscoelastic property of tissue has possibility to provide useful information for clinical imaging applications. The large attenuation effects in MRE can have a significant impact in some areas ([1]), and visualizing viscosity information has been tried for MRE ([21], [24], [25]). Fig. 12 shows the recovered viscoelastic modulus images using the direct inversion, the recovered μ^* using the gradient component of the stress wave and the fourth-updated one using the proposed algorithm, respectively. Comparing the reconstructed viscoelastic images, the proposed algorithm provided clear edge information of the inclusions and viscosity values in the inclusion seemed to be slightly larger than background viscosity value. Imaging the viscoelastic properties of tissue is, however, more easily affected by the measured noise, thus more rigorous investigation and real experiments will be necessary in future studies.

In this paper, we neglected the effect of $\nabla((\lambda + \mu)\nabla \cdot \mathbf{u})$ in the proposed reconstruction algorithm for the shear modulus. To observe the effect, we simulated the displacement field in the two dimensional domain $\Omega = (0, 10) \times (0, 10)$ cm^2 with frequency 60 Hz and didn't add random noise to the simulated displacement data. The governing elasticity system (1) can be expressed in mixed form([19]):

$$\begin{gathered} \nabla \cdot ((\mu+i\omega\zeta)\nabla\mathbf{u})+\nabla(\mu\nabla \cdot \mathbf{u})+\nabla p+\omega^2\mathbf{u}=0 \quad \text{in } \Omega \\ p=\lambda\nabla \cdot \mathbf{u} \quad \text{in } \Omega \\ u_1=1 \quad \text{on } y=10 \quad \text{and } u_1=0 \quad \text{on } y=0 \end{gathered} \quad (24)$$

We took four anomalies with different shear modulus values μ = 3 kPa and ζ = 15 Pa with the background μ = 1 kPa and ζ = 5 Pa. The second Lamé parameter λ = 1 GPa in Ω. Fig. 13(a), (b) and (c) display the displacement u_1, u_2 and the pressure p respectively with the boundary condition u_1 = 1 on the upper boundary, u_1 = 0 on the bottom boundary and Neumann values are zero on the other boundary. Fig. 14(a) shows the reconstructed shear modulus image using the direct inversion algorithm (3), (b) and (c) are reconstructed images μ^* and μ^4 using (15) and (16), respectively. In this numerical example, we found no severe damages in the reconstructed shear modulus images by neglecting the hydrostatic stress term in (24). However, to understand precisely the relation between the shear modulus and the hydrostatic stress term, more rigorous analysis will be needed including the hydrostatic stress, the shear modulus distribution, Lamé parameter λ, boundary condition, etc.

V. CONCLUSION

We propose a new inversion algorithm to reconstruct shear modulus images for MRE. The proposed shear modulus reconstruction algorithm greatly reduces the noise sensitivity related to calculating two derivatives of the measured displacement data with the usual direct inversion algorithm. Differentiating measured displacement data u_i only once and eliminating the local homogeneity assumption in the shear modulus decomposition algorithm yield more uniform estimates of the shear modulus, better noise tolerance and higher resolution in the shear modulus image.

References

1. Bishop J, Poole G, Leitch M, Plewes D. Magnetic resonance imaging of shear wave propagation in excised tissue. J Magn Reson Imaging. 1998; 8:1257–1265. [PubMed: 9848738]
2. Burlew MM, Madsen EL, Zagzebski JA, Banjavic RA, Sum SW. A new ultrasound tissue equivalent material. Radiology. 1980; 134:517–520. [PubMed: 7352242]
3. Gilbarg, D.; Trudinger, NS. Elliptic partial differential equations of second order. 2. Vol. Chapter 4. Springer-Verlag;
4. Kallel F, Bertrand M. Tissue elasticity reconstruction using linear perturbation method. IEEE Trans Med Imag. 1996; 15:299–313.
5. Kallel F, Cespedes I. Determination of elasticity distribution in tissue from spatio-temporal changes in ultrasound signals. Acoustical Imaging. 1995; 22:433–443.
6. Krouskop TA, Wheeler TM, Kallel F, Garra BS, Hall T. The elastic moduli of breast and prostate tissues under compression. Ultrason Imaging. 1998; 20:151–159. [PubMed: 9921616]
7. Kruse SA, Smith JA, Lawrence AJ, Dresner MA, Manduca A, Greenleaf JF, Ehman RL. Tissue characterization using magnetic resonance elastography: preliminary results. Physics in Medicine and Biology. 2000; 45:1579–1590. [PubMed: 10870712]
8. Manduca A, Oliphant TE, Dresner MA, Mahowald JL, Kruse SA, Amromin E, Felmlee JP, Greenleaf JF, Ehman RL. Magnetic resonance elastography: Non-invasive mapping of tissue elasticity. Medical Image Analysis. 2001; 5:237–254. [PubMed: 11731304]
9. Manduca A, Oliphant TE, Lake DS, Dresner MA, Ehman RL. Characterization and evaluation of inversion algorithms for MR elastography. Proceedings of the SPIE - The International Society for Optical Engineering. 2002; 4684:1180–1185.
10. Manduca A, Oliphant TE, Lake DS, Dresner MA, Ehman RL. Spatio-Temporal directional filtering for improved inversion of MR Elastography Images. Medical Image Analysis. 2003; 7:456–473.
11. Mathupillai R, Lomas DJ, Rossman PJ, Greenleaf JF, Manduca A, Ehman RL. Magnetic resonance elastography by direct visualization of propagating acoustic strain waves. Science. 1995; 269:1854–1857. [PubMed: 7569924]
12. Oliphant, TE.; Manduca, A.; Greenleaf, JF.; Ehman, RL. Direct, fast estimation of complex-valued stiffness for magnetic resonance elastography. Proc 8th Annual Meeting ISMRM; Denver. 2000. p. 540
13. Oliphant, TE.; Kimmick, RR.; Manduca, A.; Ehman, RL.; Greenleaf, JF. An error analysis of Helmholtz inversion for incompressible shear, vibration elastography with application to filter design for tissue charecterization; IEEE Ultrasonics Symposium; 2000. p. 1795-1798.
14. Oliphant, TE. PhD thesis. 2001. Direct methods for dynamic elastography reconstructions: Optimal inversion of the interior Helmholtz problem. submitted to Mayo Graduate School
15. Oliphant TE, Manduca A, Ehman RL, Greenleaf JF. Complex-valued stiffness reconstruction for magnetic resonance elastography by algebraic inversion of the differential equation. Magnetic Resonance in Medicine. 2001; 45:299–310. [PubMed: 11180438]
16. Ophir J, Cespedes I, Ponnekanti H, Yazdi Y, Li X. Elastography: A quantitative method for imaging the elasticity of biological tissues. Ultrasonic Imaging. 1991; 13:111–134. [PubMed: 1858217]

17. Ophir J, Cespedes I, Garra B, Ponnekanti H, Huang Y, Maklad N. Elastography: ultrasonic imaging of tissue strain and elastic modulus in vivo. European J Ultrasound. 1996; 3:49–70.
18. Ophir J, Alam S, Garra B, Gallel F, Konofagou E, Krouskop T, Merritt C, Righetti R, Souchon R, Srinivasan S, Varghese T. Elastography: Imaging the elastic properties of soft tissues with ultrasound. J Med Ultrasonics. 2002; 29:155–171.
19. Park E, Maniatty M. Shear modulus reconstruction in dynamic elastography: time harmonic case. Physics in Medicine and Biology. 2006; 51:3697–3721. [PubMed: 16861775]
20. Romano A, Bucaro J, Ehman RL, Shirron J. Evaluation of a material parameter extraction algorithm using MRI-based displacement measurements. IEEE Trans Ultrason Ferroelect Freq Control. 2000; 47:1575–1581.
21. Sack I, Beierbach B, Hamhaber U, Klatt D, Braun J. Non-invasive measurement of brain viscoelasticity using magnetic resonance elastography. NMR in Biomedicine. 2008; 21:265–271. [PubMed: 17614101]
22. Papazoglou S, Hamhaber U, Braun J, Sack I. Algebraic Helmholtz inversion in planar magnetic resonance elastography. Physics in Medicine and Biology. 2008; 53:3147–3158. [PubMed: 18495979]
23. Sinkus R, Lorenzen J, Schrader D, Lorenzen M, Dargatz M, Holz D. High-resolution tensor MR elastography for breast tumor detection. Phys Med Biol. 2000; 45:1649–1664. [PubMed: 10870716]
24. Sinkus R, Tanter M, Xydeas T, Catheline S, Bercoff J, Fink M. Viscoelastic shear properties of in vivo breast lesions measured by MR elastography. J Magn Reson Imaging. 2005; 23:159–165.
25. Xydeas T, Siegmann K, Sinkus R, Krainick-Strobel U, Miller S, Claussen CD. Magnetic resonance elastography of the breast: correlation of signal intensity data with viscoelastic properties. Invest Radiol. 2005; 40:412–420. [PubMed: 15973132]
26. Van Houten E, Paulsen KD, Miga MI, Kennedy FE, Weaver JB. An overlapping sub zone technique for MR based elastic property reconstruction. Magn Reson Med. 1999; 42:779–786. [PubMed: 10502768]
27. Van Houten E, Miga M, Weaver J, Kennedy F, Paulsen K. Three-dimensional subzone-based reconstruction algorithm for MR elastography. Magn Reson Med. 2001; 45:827–837. [PubMed: 11323809]
28. Yin M, Talwalkar JA, Glaser KJ, Manduca A, Grimm RC, Rossman PJ, Fidler JL, Ehman RL. Assessment of hepatic fibrosis with magnetic resonance elastography. Clin Gastroenterol Hepatol. 2007; 5:1207–1213. [PubMed: 17916548]

Appendix

In this appendix, we investigate the behavior of ∇h_i inside $\mathcal{R}$ when h_i is a solution of (8) with a oscillating boundary data $\frac{\partial h_i}{\partial \nu}$ having zero mean on the boundary $\partial\mathcal{R}$. From the basic theory of elliptic partial differential equations (Gilbarg and Trudinger 1983), the potential functions h_i, $i = 1, 2, 3$ can be expressed as

$$h_i(\mathbf{r}) = \int_{\partial\mathcal{R}} \frac{\partial \Phi(\mathbf{r}-\mathbf{r}')}{\partial \nu} h_i \, ds - \int_{\partial\mathcal{R}} \Phi(\mathbf{r}-\mathbf{r}') \frac{\partial h_i(\mathbf{r}')}{\partial \nu} ds \quad (25)$$

where $\Phi(\mathbf{r}-\mathbf{r}') = -\frac{1}{4\pi}\frac{1}{|\mathbf{r}-\mathbf{r}'|}$ in three dimensional case and $\Phi(\mathbf{r}-\mathbf{r}') = \frac{1}{2\pi}\log(|\mathbf{r}-\mathbf{r}'|)$ in two dimensional case. Due to the harmonic force inside $\mathcal{R}$ which means that the harmonic function h_i has average property inside $\mathcal{R}$, the highly oscillating values on the boundary rapidly vanishes inside the region. Fig. 11 shows this effect where we take a highly oscillating Neumann boundary condition ranging from −0.4 to 0.4 as shown in Fig. 11(a). The image of the resulting harmonic solution shown in Fig. 11(b) indicates that the random noise effects rapidly decaying inside the region and $|h_i| < 0.004$ inside the region.

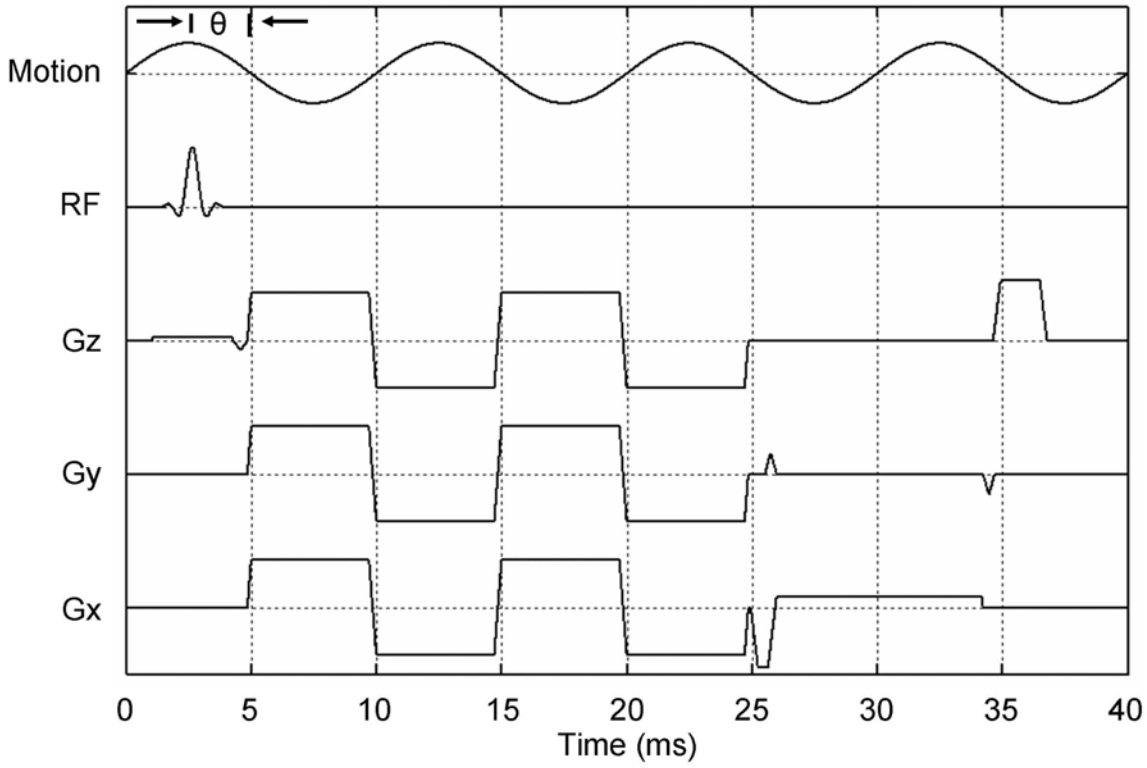

Fig. 1.
Gradient echo MRE pulse sequence. The motion-sensitizing gradients are applied along any direction. By changing the sign of the motion-sensitizing gradients, a phase difference image can be produced.

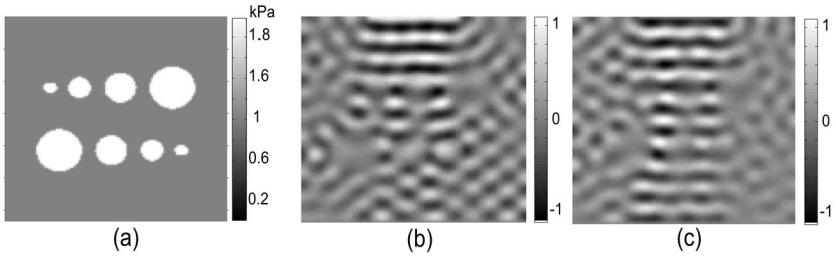

Fig. 2. Simulation setup

(a) is the target shear modulus image.

(b) and (c) are the real and imaginary part of the simulated displacement images, respectively.

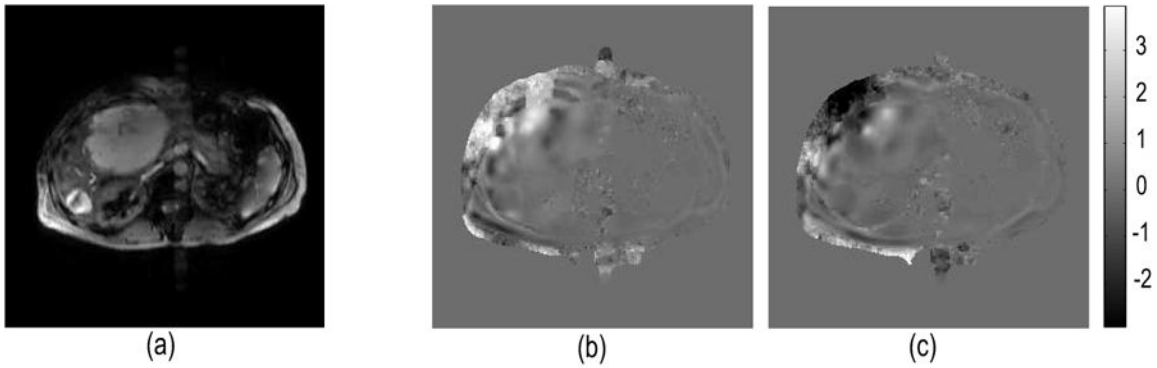

Fig. 3. Liver MRE data for a patient with multiple hepatic lesions

(a) is a GRE MRE axial magnitude image of a slice including two lesions: a large lesion in the anterior portion of the liver and a smaller lesion in the posterior portion.

(b) and (c) show the real and imaginary parts of the through-plane component of the measured harmonic wave field indicating the wave propagation in this patient.

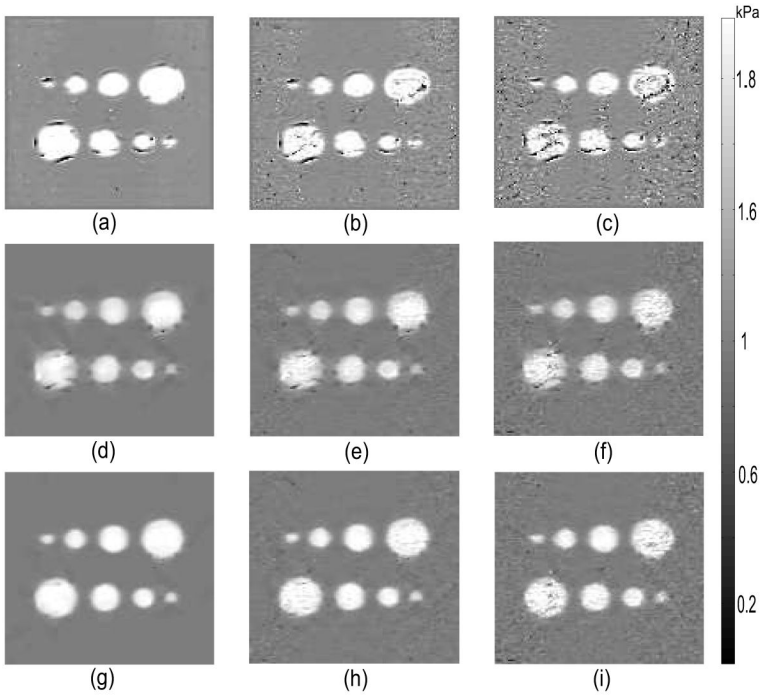

Fig. 4.

Simulation results. The first row shows the reconstructed shear modulus images using the direct inversion algorithm. The second and third rows show μ^* and μ^4 images using the gradient component of stress based inversion algorithm. The first, second and third columns are recovered with displacement data containing noiseless, 2%, and 4% random noise, respectively.

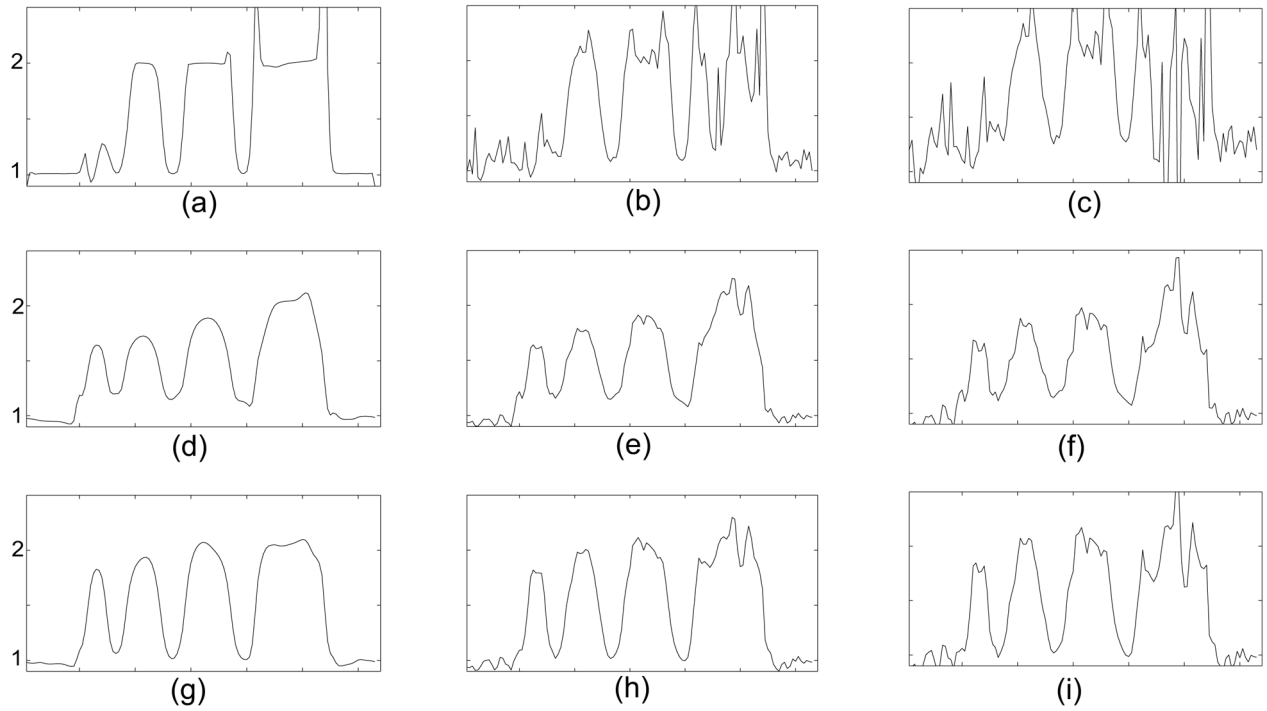

Fig. 5.
Profile lines of the reconstructed shear modulus images in Fig. 4.

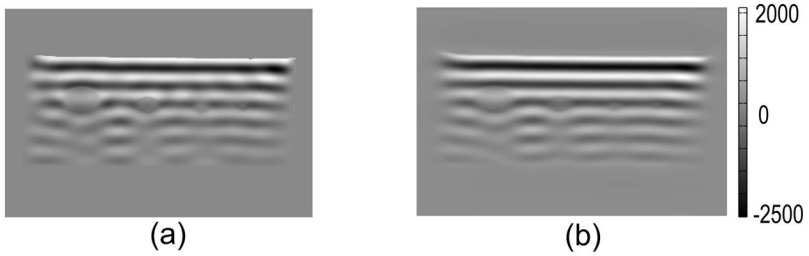

Fig. 6. Phantom displacement images

(a) is the measured displacement image.

(b) is the corresponding directional filtered image.

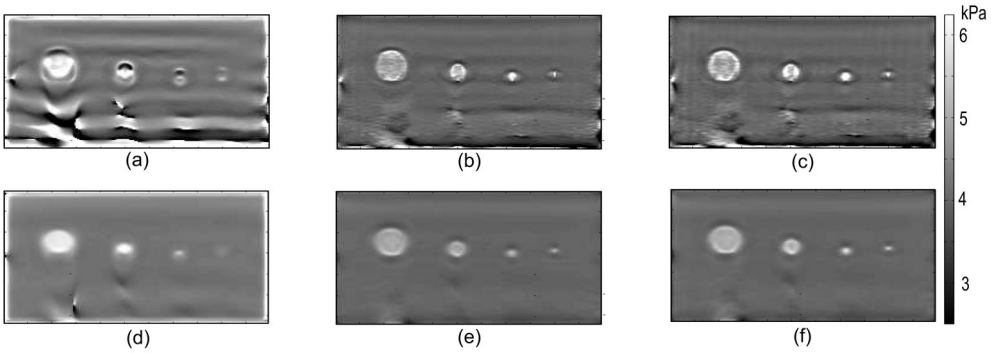

Fig. 7. Results from the phantom study

(a), (b) and (c) are reconstructed shear modulus images using the original measured displacement data.

(d), (e) and (f) are the corresponding images using the directionally filtered displacement data.

Column 1 shows results from the direct inversion algorithm, while columns 2 and 3 show μ^* and μ^4 from the proposed algorithm.

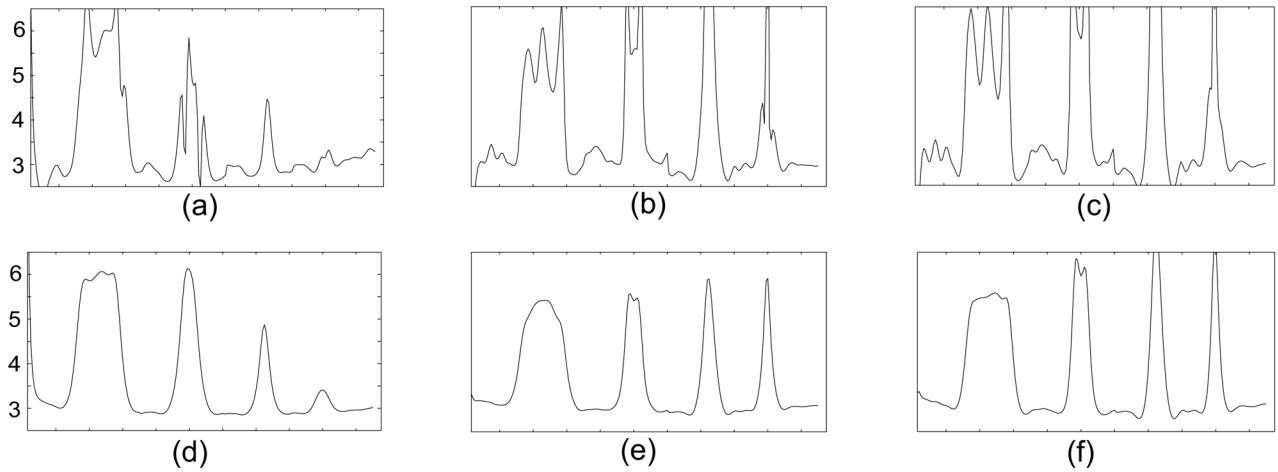

Fig. 8. Profiles through the four inclusions from the results shown in Fig. 7

(a–c) are the profiles without filtering data using the direct inversion method and the gradient component of stress based method(μ^* and μ^4), respectively.

(d–f) are the corresponding profiles with the directionally filtered data.

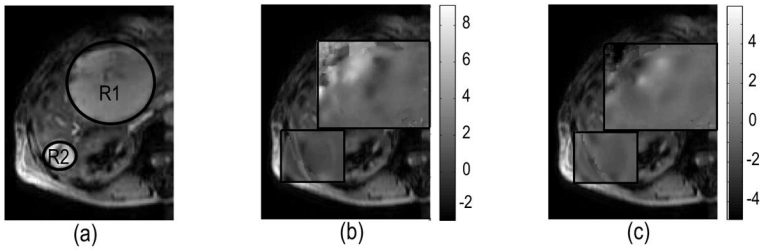

Fig. 9. In vivo human liver experiment results

Two circles in the magnitude image (a) denote the tumor region.
(b) and (c) are the real and imaginary part images of the potential function in two local regions by solving the elliptic equation (6) with the measured displacement data as a source term.

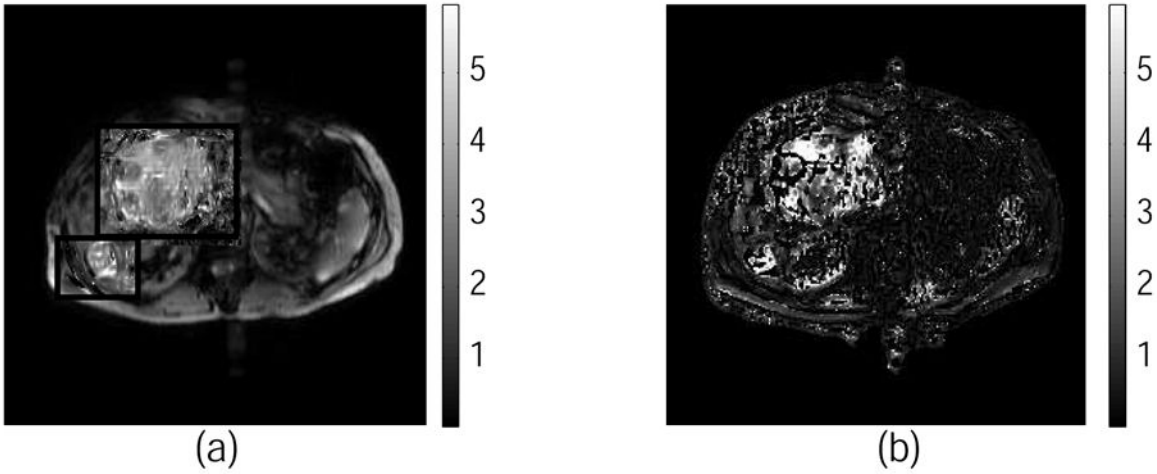

Fig. 10. In vivo human liver experiment results

(a) and (b) are the reconstructed shear modulus images using the gradient component of stress based inversion algorithm and the direct inversion algorithm, respectively.

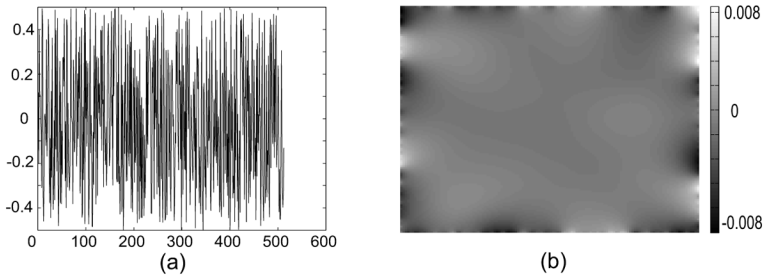

Fig. 11.

(a) is highly oscillating Neumann boundary data following the boundary of the region $(0, 1)^2$.

(b) is the corresponding harmonic solution.

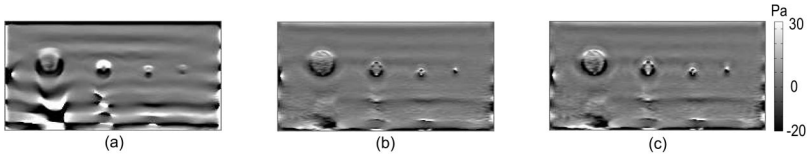

Fig. 12.

(a), (b) and (c) are reconstructed visco-elastic images with the original measured displacement data using the direct inversion method, the reconstructed one using the gradient component of stress and the fourth-updated one using the shear modulus decomposition algorithm, respectively.

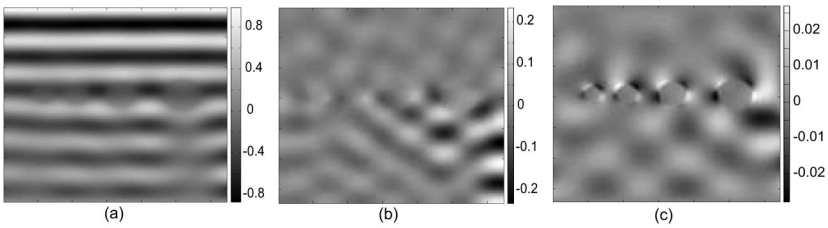

Fig. 13.
(a) and (b) are real part of the displacement data u_1 and u_2. (c) is real part of the pressure.

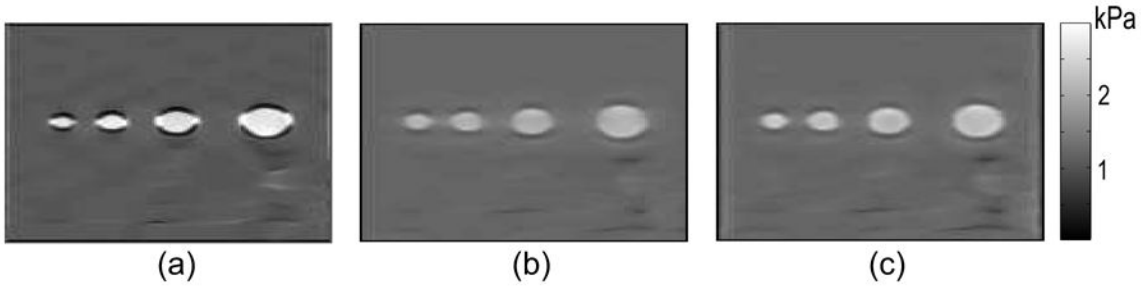

Fig. 14.

(a), (b) and (c) are reconstructed shear modulus images with the displacement data by solving the elasticity system (24).

(a) shows the shear modulus image from the direct inversion algorithm, while (b) and (c) show μ^* and μ^4.

Table 1

Relative errors $E_{\mu}{}^{r}$ using the direct inversion algorithm ($E_{\mu}{}^{DI}$) and the proposed gradient component of stress based algorithm ($E_{\mu}{}^{*}$, $E_{\mu}{}^{i}$, $i = 1, \cdots, 4$) with noiseless data and noisy data.

	$E_{\mu}{}^{DI}$	$E_{\mu}{}^{*}$	$E_{\mu}{}^{1}$	$E_{\mu}{}^{2}$	$E_{\mu}{}^{3}$	$E_{\mu}{}^{4}$
0%	0.1653	0.1027	0.0798	0.0711	0.0671	0.0651
2%	0.2323	0.1099	0.0902	0.0828	0.0793	0.0746
4%	0.3116	0.1276	0.1135	0.1086	0.1063	0.1051